

# Reconfigurable emulator for photovoltaic modules under static partial shading conditions



Tuan Dat Mai <sup>\*,1</sup>, Sven De Breucker <sup>2</sup>, Kris Baert <sup>1</sup>, Johan Driesen <sup>1</sup>

EnergyVille, Poort Genk 8310, 3600 Genk, Belgium<sup>3</sup>

## ARTICLE INFO

### Article history:

Received 14 July 2016

Received in revised form 25 November 2016

Accepted 28 November 2016

Available online 9 December 2016

### Keywords:

Emulator

PV generators

Real-time systems

Kalman filters

## ABSTRACT

This paper aims to emulate the *IV* characteristics of a multiple-substring photovoltaic (PV) module under nonuniform irradiance levels by taking into account the breakdown voltage of shaded cells, configurations of bypass diode connections, and cell temperatures. A suitable control scheme for the emulator's power stage significantly improves the performance of the emulator's output. As a result, this PV emulator proves to be capable of performing under various operating conditions of the PV module including uniform irradiation and nonuniform partial shading with great accuracy.

© 2016 Elsevier Ltd. All rights reserved.

## 1. Introduction

Reproducing the current–voltage (*IV*) characteristics of a PV module under different environmental conditions is challenging and time-consuming in a laboratory set-up (Woyte et al., 2003). Therefore, a PV emulator, which is a programmable power system duplicating the electrical *IV* characteristics of a given PV module at an emulator's output, provides a useful test facility solution for PV applications. Thirty years ago, the first generations of PV emulators were developed by implementing analog circuits (Vachtsevanos and Kalaitzakis, 1987). PV cell and module emulators have been studied since then. The PV emulators are classified into two groups: (1) few watt emulator systems (Wandhare and Agarwal, 2011; Schofield et al., 2011); (2) hundred-to-few kilowatt emulator systems (Martín-Segura et al., 2007; Kadri et al., 2010; Dolan et al., 2011; Abidi et al., 2012; Lu and Nguyen, 2012; Agrawal and Aware, 2012; Kim et al., 2013; Koran et al., 2014; Erkaya et al., 2015; Balato et al., 2016). These two categories also reflect the primary purpose of using the emulator which can be PV cell or PV module/array emulation.

Recent research also raises great interest in the study of PV behavior under partial shading conditions. This implies that the developed PV emulators should be capable of emulating more complicated test cases with appropriate transient responses. The PV module, in general definition, consists of substrings with an equal number of cells. When some of the PV cells are not fully illuminated compared to other cells, the partial shading effect causes mismatch in the PV module. Although bypass diodes connected in parallel to the substrings block high negative voltages across each substring, individual shaded cells in a substring can cause a significant decrease in energy yield and multiple power peaks (Woyte et al., 2003).

The development of partial shading PV emulators has been proposed in recent times in several studies regarding power electronic converters for decentralized PV systems and the question is whether the designed converters can steadily deliver the highest PV power/energy to the output under nonuniform irradiance conditions. These PV emulators emulate partially shaded PV modules with different approaches to produce the *IV* curves. The first approach uses a look-up-table method where a discrete and limited amount of data of *IV* curves in given shading conditions can be found in commercial products such as Chroma (2012). In the second approach, a multi-*IV* circuit magnifies the small *pn* photo-sensor output by analog technology (Nagayoshi, 2004; Koran et al., 2014) which provides little or no flexibility of PV characteristics and bypass diode configurations. In the third approach, model-based PV emulators at different environmental and shading conditions are taken into consideration (Di Piazza and Vitale, 2010; Kadri et al., 2010; Chroma, 2012; Heredero-Peris et al., 2014).

\* Corresponding author.

E-mail addresses: [tuandat.mai@esat.kuleuven.be](mailto:tuandat.mai@esat.kuleuven.be) (T.D. Mai), [sven.debreucker@vito.be](mailto:sven.debreucker@vito.be) (S. De Breucker), [kris.baert@esat.kuleuven.be](mailto:kris.baert@esat.kuleuven.be) (K. Baert), [johan.driesen@esat.kuleuven.be](mailto:johan.driesen@esat.kuleuven.be) (J. Driesen).

<sup>1</sup> Electrical Engineering Department (ESAT), KU Leuven.

<sup>2</sup> Unit Energy Technology (ETE), Flemish Institute for Technological Research (VITO).

<sup>3</sup> EnergyVille is an association of the Flemish research institutes KU Leuven<sup>1</sup>, VITO<sup>2</sup> and IMEC in the field of sustainable energy and smart energy systems.

These modeling methods, however, show several limitations in either modeling the negative breakdown voltage or/and different configurations of partially shaded substrings. The complexity of the *IV* curves also leads to the deterioration of the output performance in the emulators when partially shaded PV emulation is activated. To mitigate the limitations of previous methods, there is an urgent need to build a PV emulator capable of performing well under partial shading conditions such as in complex urban areas where influential environmental parameters including cell temperature and solar irradiation conditions are separately defined for each PV cell.

The emulator proposed in this paper is designed to tackle such issues. The modeling of a partially shaded PV module involves extracting *IV* characteristics from cell-level parameters such as temperatures, irradiance levels, and breakdown voltage (Díaz-Dorado et al., 2014; Quaschnig and Hanitsch, 1996; Patel and Agarwal, 2008). The modeling of PV module substring configurations and bypass diodes under partial shading scenarios are also discussed. For high operation quality, measurement errors and control delays caused by sensors and analog-to-digital interfaces are mitigated by introducing the Kalman filter (KF) approach.

This paper is organized into four sections. In Section 2, the PV modeling and implementation methodology is presented. A mathematical PV model is derived from the solar cell level to the PV module level. Hardware connection diagrams, a real-time measurement technique, and a hybrid control strategy are also presented. Section 3 introduces experimental tests of the emulator performed on an electronic load and a DC demonstration board to assess the emulator's operation. Finally, a summary of our work is presented in Section 4.

## 2. Methodology

### 2.1. PV module modeling

As the smallest elements of a PV module, the PV cells directly convert solar irradiation to electricity due to the photovoltaic effect. The power produced by each cell depends on operating points along the *IV* curve, temperature, irradiation, and PV technology. Therefore, the modeling of PV cells is the core element for emulating the whole PV module in this study.

#### 2.1.1. Modeling of a solar cell with consideration of the avalanche breakdown

The proposed equivalent circuit of a PV cell in Fig. 1 refers to a single-diode model and a current source representing the avalanche breakdown behavior, which has been validated for modeling PV cells in literature (Silvestre et al., 2009; Ishaque et al., 2011).

$$I_{cell} = \underbrace{\frac{S}{S_n}(I_{ph,0} + K_I \Delta_T)}_{I_{ph}} - \underbrace{I_0 \left[ \exp \left( \frac{V_{cell} + I_{cell} R_s}{\frac{n k T}{q}} \right) - 1 \right]}_{I_d} - \underbrace{\frac{V_{cell} + I_{cell} R_s}{R_p}}_{I_{sh}} - \underbrace{a(V_{cell} + I_{cell} R_s) \left( 1 - \frac{V_{cell} + I_{cell} R_s}{V_{br}} \right)^{-m}}_{I_{br}} \quad (1)$$

Eq. (1) describes the *IV* characteristic of a PV cell including the avalanche breakdown. The first three terms, namely the light-generated current  $I_{ph}$ , *pn* junction current  $I_d$ , and shunt-resistance leakage current  $I_{sh}$  express the single-diode model of a PV cell (Vachtsevanos and Kalaitzakis, 1987). The last term, controlled current source  $I_{br}$ , is added into the original one-diode model to describe the avalanche breakdown in the case of high reverse-bias voltage (Quaschnig and Hanitsch, 1996; Kawamura et al., 2003; Díaz-Dorado et al., 2014).

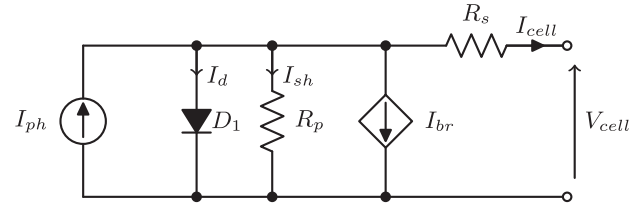


Fig. 1. Model of one-diode PV cell with current source  $I_{br}$  generating avalanche breakdown at high negative voltages.

In the case of the PV cell model introduced in (1),  $I_{ph,0}$  is the light-generated current at the standardized condition (STC).  $S/S_n$  represents the ratio of the cell irradiance level ( $S$ ) to 1000 W/m<sup>2</sup> that is the STC irradiance levels.  $\Delta_T = T - T_{25}$  is the difference between the actual and STC cell temperatures.  $I_0$  denotes the reverse saturation current for an ideal *pn*-junction diode,  $n$  is the diode ideality factor.  $R_s$  and  $R_p$  are respectively the cell series resistance and shunt resistance of a PV cell under identical temperature values.  $q$  is the elementary charge.  $k$  is the Boltzmann's constant, and  $T$  is the cell temperature (in Kelvin).

In the case of diode breakdown at a high negative voltage,  $V_{br}$  describes the avalanche breakdown voltage.  $a$  represents the correction factor and is often less than 1 Ω<sup>-1</sup> (Quaschnig and Hanitsch, 1996). The parameter  $m$  denotes the avalanche breakdown exponent. These parameters are estimated from the measurement of a PV module (Kawamura et al., 2003).

Given that environmental parameters including  $S$  and  $T$  can be set by users and the other parameters are defined in the datasheet, the combinations of  $n$ ,  $R_s$ , and  $R_p$  have to be estimated to obtain the *IV* characteristics of cells in a PV module.

By applying the fast-convergence method illustrated in Carrero et al. (2011) to estimate PV parameters from the given datasheet,  $I_{ph,0}$ ,  $I_0$ ,  $R_s$ ,  $R_p$ , and  $n$  during environmental conditions are specified. The *IV* characteristic is hence obtained by applying (1) and the sweeping current from zero to the short-circuit current corresponding to the highest irradiance level over a substring, which also defines the negative voltage area of the PV cells.

$$I_{cell} = g(V_{cell}, S) \quad (2)$$

For a substring comprising  $N_s$  uniformly irradiated cells in series and operating at the same cell temperature  $T$ , it is feasible to extend the expression of a single cell to the following substring equations:

$$\left. \begin{aligned} I_{substring} &= I_{cell} \\ V_{substring} &= N_s \times V_{cell} \end{aligned} \right\} \Rightarrow I_{substring} = g\left(\frac{V_{substring}}{N_s}, S\right) \quad (3)$$

Modeling *IV* characteristics under uniform irradiation ( $S$ ) is validated through the datasheet of PV module KC200GT (Kyocera, 2009). Results of the comparison are depicted in Fig. 2. Under high irradiation levels, the obtained *IV* curves fit the experimental ones over all temperature ranges. Under low irradiation levels, although the voltage slightly deviates from the experimental data near the open-circuit voltage area, the relative error of maximum power remains low at 1% as mentioned in Ishaque et al. (2011). In addition, the calculation time of the single-diode model approach is approximately 1.6 times shorter than the calculation time of the two-diode model (Ishaque et al., 2011). Therefore, subjected to multiple PV cell modeling under different environmental conditions, the computational time for estimating typical *IV* characteristics of cells is reduced.

Finally, the characteristics of cells are extrapolated in accordance with the working conditions of cell irradiance levels and temperatures to obtain the *IV* characteristics under given partial shading conditions. The *IV* curve of the module is subsequently

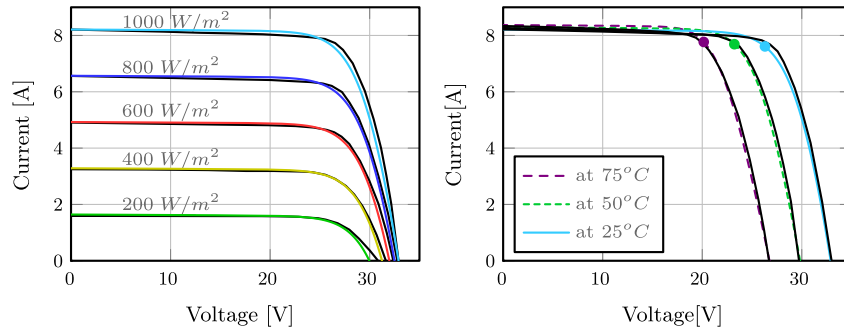


**Fig. 2.** IV characteristics for the 60-cell PV module Kyocera KC200GT obtained from datasheet (black) and modified single-diode model (color) (Kyocera, 2009). (For interpretation of the references to color in this figure legend, the reader is referred to the web version of this article.)

obtained by combining cells' characteristics and bypass diode configurations. When the obtained IV curve is emulated, the emulator offers to assess the maximum power-point tracking (MPPT) and power/energy yield efficiency of converters without significant power deviation from real PV modules.

### 2.1.2. Modeling IV characteristics at substring level

A bypass diode can be wired across each substring as illustrated in Fig. 3. An example of a substring connection in the 60-cell PV module KC200GT is shown in Fig. 4(a) where three groups of 20 cells are irradiated by different uniform irradiance levels. The characteristics of separate cells obtained from the previous modeling step are mathematically grouped to model the IV characteristics of the substrings.

The purpose of the bypass diodes in an PV module is to eliminate the hot spot formation by drawing the current away from shadowed strings (Patel and Agarwal, 2008; Díaz-Dorado et al., 2014). When the string current exceeds the short-circuit substring current, the bypass diode starts conducting to carry the majority of the PV module current. The IV characteristics of different substrings under nonuniform shading conditions are not the same as that of substrings under uniform irradiation. Hence, the modeling



**Fig. 3.** Connection diagram of a PV substring with a bypass diode bridge.

of IV characteristics of substrings with and without a bypass diode is explicitly described in following subsections.

### 2.1.3. Modeling a substring without bypass diode connection

It is assumed that the IV characteristic of the  $k$ th cell is established by the modeling procedure in Section 2.1. When the function  $\mathbf{g}(V_{\text{cell}}, S)$  is extended to multiple cell modeling, the IV characteristic of the  $k$ th cell can be described as follows:

$$\begin{cases} I_{\text{cell},k} = \mathbf{g}_k(V_{\text{cell},k}, S_k) \\ V_{\text{cell},k} = \mathbf{g}_k^{-1}(I_{\text{cell},k}, S_k) \end{cases} \quad (4)$$

where the subscript ' $k$ ' denotes the cell  $k$  located in the PV module.

In a multiple-string PV module subjected to nonuniform irradiation, the shadowed substrings generate lower output voltage as compared to full-illuminated ones at the same substring current. The substrings irradiated by low irradiance levels shift to the negative voltage area when the substring current starts being higher than their short-circuit currents (Kawamura et al., 2003). As illustrated in Fig. 3, cells numbered  $k$  to  $j$  are grouped in a substring. The voltage across the substring at a given current value  $I_{\text{substring}}$  is explicitly equal to the sum of the cell voltages as follows:

$$\begin{cases} I_{\text{substring}} = I_{\text{cell},j} = \dots = I_{\text{cell},k} = I \\ V_{\text{substring}} = \sum_{i=k}^j V_{\text{cell},i} = \sum_{i=k}^j \mathbf{g}_i^{-1}(I_{\text{cell},k} = I, S_i) \end{cases} \quad (5)$$

By using the sequential superposition algorithm, the substring comprising cells  $k$  to  $j$  is derived from the following function  $\mathbf{f}$ .

$$\mathbf{f} = \sum_{i=k}^j \mathbf{g}_i \Rightarrow I_{\text{substring}} = \mathbf{f}(V_{\text{substring}}) \quad (6)$$

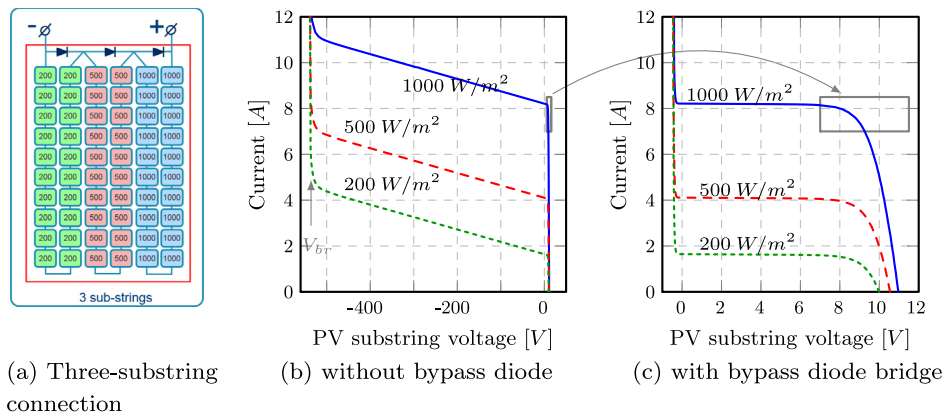


**Fig. 4.** Configuring a PV module KC200GT in the three-substring connection (a) and modeling IV characteristics of a 20-cell substring at 200 (green), 500 (red), and 1000 W/m² (blue) without (b) and with (c) bypass diode. (For interpretation of the references to color in this figure legend, the reader is referred to the web version of this article.)

Fig. 4(b) shows the *IV* characteristics of separate 20-cell PV substrings without a bypass diode. Due to avalanche breakdown, PV substring currents exponentially increase close to the breakdown voltage. This is only seen in Fig. 4 at a given cell temperature and sunlight spectrum; the currents are lower at low irradiance levels than at full irradiance levels.

#### 2.1.4. Modeling the *IV* characteristics of a PV module with bypass diodes

The effects of bypass diodes are vital for modeling the *IV* characteristics of a multiple substring PV module (Ishaque et al., 2011). By applying Kirchhoff's current law for a substring of PV cells connected in parallel with a bypass diode, the main feeder current is derived as follows:

$$I_{\text{substring}} + I_{bp} = I_{\text{module}}, \quad (7)$$

where  $I_{bp}$  denotes the diode forward current, and  $I_{\text{module}}$  denotes the current measured at the output terminal of the PV module.

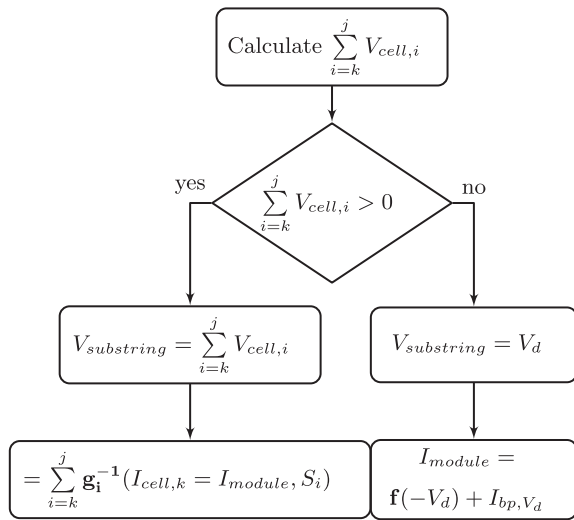


Fig. 5. Flowchart of extrapolating to a PV substring bridged by a bypass diode. According to Fig. 3, cells  $k$  and  $j$  are the 1st and the last cells in the given substring, respectively.

The diode equation is derived in Ishaque et al. (2011) as follows:

$$I_{bp} = I_{0d} \left[ \exp \left( \frac{-qV_d}{k_B T_d} \right) - 1 \right], \quad (8)$$

where  $V_d$  is the forward diode voltage and is equal to  $-V_{\text{substring},a}$  in this substring connection.  $I_{0d}$ ,  $k_B$ , and  $T_d$  are the diode parameters respectively.

The numerical solution to simulate the *IV* curve of a substring with a bypass diode is described by the flowchart in Fig. 5. The *IV* characteristics of a 20-cell PV substring wired through a bypass diode is derived and plotted under three solar irradiance levels. In comparison to Fig. 4(b) where bypass diodes are not introduced, the implementation of bypass diodes in Fig. 4(c) clamps the negative voltage of the 20-cell PV substrings at the forward diode voltage, which is assumed to be significantly less than the PV cell breakdown voltage. The substring with and without bypass exhibit the same *IV* characteristics at the positive substring voltage area.

## 2.2. System description and operation strategy

### 2.2.1. System description

The system diagram of the developed PV emulator is shown in Fig. 6. The supervisory layer, which enables a graphical user interface in the MATLAB environment, performs the modeling of PV module's *IV* curves, the calculation of PV emulator's control parameters, and the compilation to C-code. The Xenomai real-time Target (RTT) applies control references to the 100 V–13 A programmable power supply (PPS) according to feedback measurements and emulation strategies given by the high-level control. Because the RTT and the PPS communicate using analog signals, analog-to-digital and digital-to-analog conditioning devices are implemented as the signal conditioning layer. The PPS sets the reference values to its output, and returns the feedback measurements.

### 2.2.2. Control strategy

The *IV* characteristic of a PV module under a given uniform irradiation condition is a nonlinear curve, especially around the MPP (Villalva et al., 2009). However, sections of the *IV* curve are almost linear when the PV module exhibits operating points near  $V_{oc}$  or  $I_{sc}$ . According to Yuan et al. (2009); Di Piazza and Vitale (2010); Kim et al. (2013), a hybrid control scheme is considered as a suitable solution for PV emulators. Current control is employed when the

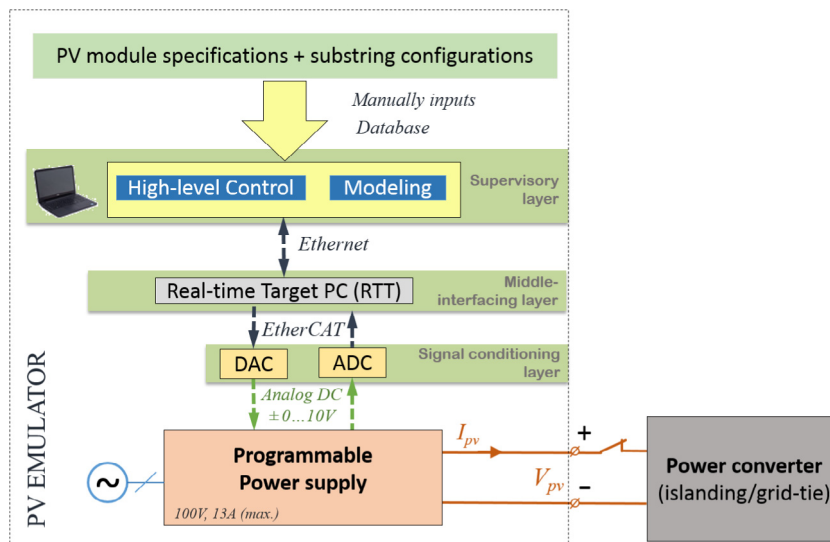


Fig. 6. Block diagram of the developed PV emulator.



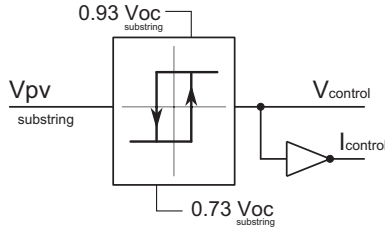


Fig. 7. Hybrid control mode for PV control reference.

current is less than  $I_{mpp}$  and the voltage ranges between  $V_{mpp}$  and  $V_{oc}$ . Alternatively, voltage control is activated when the PV current nearly reaches  $I_{sc}$ .

In this work, an extension of the controller based on a simple hysteresis procedure is implemented as shown in Fig. 7. This additional control block eliminates nuisance switching between two control modes that is caused by measurement errors around the switching points (Yuan et al., 2009). The control mode  $V_{control}$  considers  $I_{pv}$  as measurement quantity and yields

$$V_{pv}^* = \mathbf{f}^{-1}(I_{pv \text{ measured}}) \quad (9)$$

where  $\mathbf{f}^{-1}$  denotes the IV characteristic of a PV substring calculated in (6). Alternatively, the  $I_{control}$  mode takes  $V_{pv}$  into account as measurement quantity and performs as follows:

$$I_{pv}^* = \mathbf{f}(V_{pv \text{ measured}}) \quad (10)$$

### 2.2.3. Implementing the Kalman filter for real-time measurements and a priori control set-points

In terms of control, analog interfaces enable large bandwidth communication between the PPS and the RTT. However, the received analog signals contain unpredictable noise. In addition, analog-to-digital conversion between the RTT-PPS link causes time latency, which makes values read in the RTT more delayed than the instantaneous values measured with voltage/current sensors. Meanwhile, control references transferred from the RTT to the PPS suffer from latency due to digital-to-analog conversion time. Therefore, the reference values are not actually the real-time desired references unless the a priori reference method is implemented. To resolve this problem, applying a KF is proposed in the present work to assign a priori control set-points (Franklin et al., 1990), as well as to perform real-time estimation (Dorf and Bishop, 2011). Due to the similarity approach of the KF for the measurement acquisition and the power control stage, only representative KF equations for real-time measurement are explained.

The measurement model of an electrical quantity, either current or voltage, is described as follows in the discrete-time domain:

$$\begin{aligned} z_{(k+1)} &= Az_{(k)} + Gw_{(k)} + Hu_{(k)} \\ y_{(k)} &= Cz_{(k)} \end{aligned} \quad (11)$$

where

$$z_{(k)} = [z_{(k)}; \Delta z_{(k)}]^T$$

- $z_{(k)}$  denotes the measured values at the sampling instant  $k$ .
- $y_{(k)}$  is the filtered measurement outputs.  $\Delta z_{(k)} = z_{(k)} - z_{(k-1)}$  denotes measurement variation after each sampling.
- $u_{(k)}$  and  $w_{(k)}$  are the inputs and noise values respectively.

Sensors acquire measurements which are not affected by external controls. The measurement space states, which are derived by (11), represents an autonomous system. State-matrices are hence illustrated as follows:

$$A = \begin{bmatrix} 1 & T_s \\ 0 & 1 \end{bmatrix}; G = \begin{bmatrix} 1 & 0 \\ 0 & 1 \end{bmatrix}; C = [1 \ 0]; H = \begin{bmatrix} 0 \\ 0 \end{bmatrix}; \quad (12)$$

where  $T_s$  denotes the sampling period.

The measurement and process noises are assumed to be unknown. The process and measurement noises are defined according to the specifications of hardware devices. Then, the Kalman estimator is derived so that state estimates are updated at every sampling instant (Dorf and Bishop, 2011).

## 3. Validation results and discussion

The validation procedure is conducted for the purpose of validating and evaluating thoroughly the proper function of the proposed emulator. Accordingly, two different types of power sinks including a controllable electronic load and a module-level DC/DC converter are subsequently interconnected to the emulator to assess the PV emulator's operation.

### 3.1. Operation performance of emulator interfacing with an electronic load

The interconnection diagram shown in Fig. 8 is carried out to validate the effectiveness of the proposed a priori control method and real-time estimation contributed by using the KF. The electronic load applies a sinusoidal current waveform, which is depicted in Fig. 8, from 0 A to  $I_{sc}$ . The emulator therefore responds to the load demand and emulates the characteristics of a PV module Kyocera KC200GT.

For the emulation of a uniformly irradiated PV module, the emulated IV curve in Fig. 9(a) shows a test case where the KF is not implemented. Within 7943 measured points, 297 points do not overlay on  $\pm 5\%$  margin of the desired IV characteristic, meaning that the number of points not overlaying the IV curve contributes only approximately 3.74% of the total measured points. In the case that the KF is deployed, as depicted in Fig. 9(b), there are no points outside the margin. The trajectory of the measured points closely follows the modeled IV characteristics.

A step response test is performed to evaluate the transition performance of the PV emulator. The 8.21 A current load corresponding to the short-circuit current  $I_{sc}$  is constantly connected and disconnected to the PV emulation, which is reported in Fig. 10. The resulting voltage falling time at the coupling point is less than 30 ms and faster than the implementation presented in Koran et al. (2014), which is approximately 150 ms. The current rising time is significantly faster and is approximately 4 ms when an electronic load is connected. The rising time of current requires up to 10 ms in Martín-Segura et al. (2007), demonstrating the desired performance of the proposed control strategy.

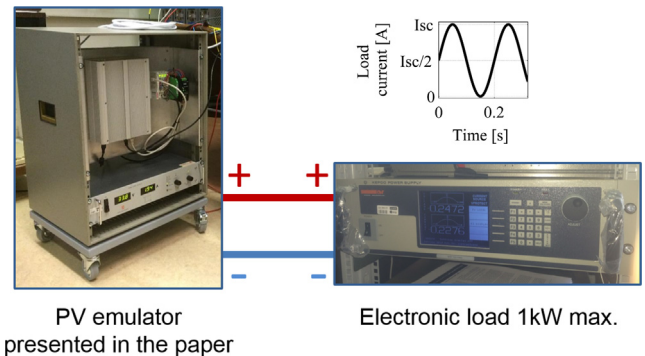


Fig. 8. Diagram of the developed PV emulator test bench interfaced to an electronic load.

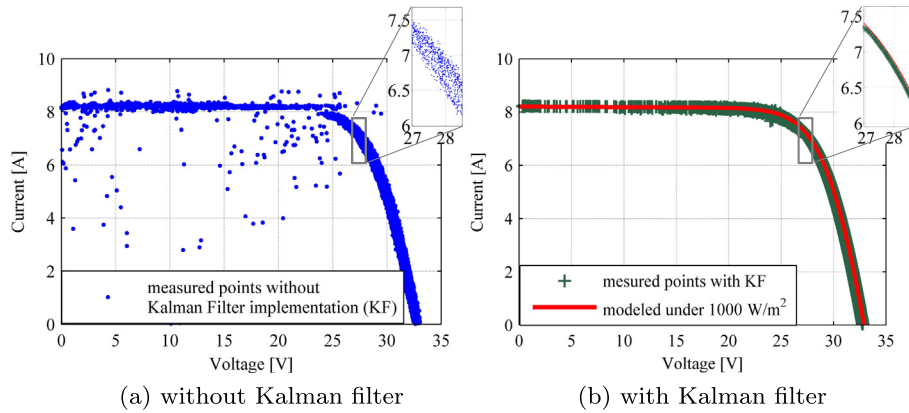


Fig. 9. The IV curve of the PV module Kyocera KC200GT emulated under a uniform irradiation condition.

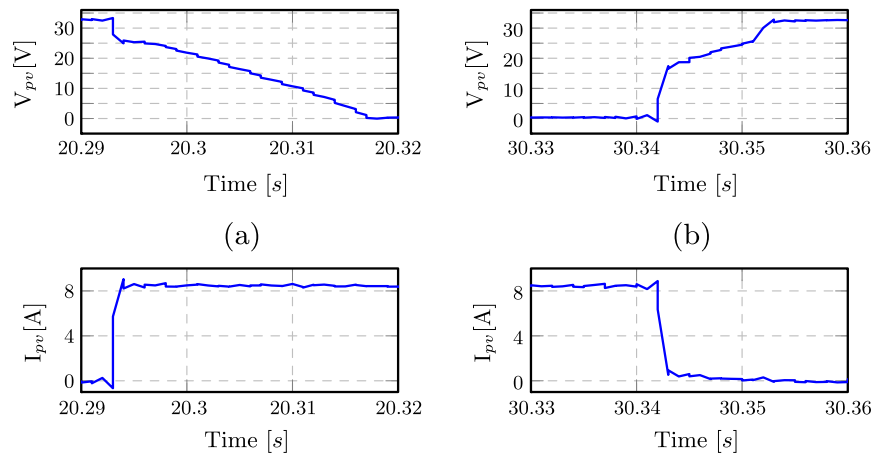


Fig. 10. Step response of the PV emulator output interfaced to a power electronic load: (a) load current  $I_{sc}$  applied; (b) load released.

To verify the simulation of a multiple-substring PV module under nonuniform irradiation conditions, scenarios of two substrings and three substrings for the PV module KC200GT were carried out. The current value of the electronic load is periodically swept from 0 to 8.21 A ( $I_{sc}$  of KC200GT module), as depicted in Fig. 10. The IV curves subjected to two and three substrings are illustrated in Fig. 11. The number of local MPPs is equal to the number of irradiance levels imposed on the PV module.

Fig. 12 demonstrates the power error of experimental points compared to the IV modeling in module and substring PV simulation cases. The error curve measured in this work is the same as that in Villalva et al. (2009). It is worth noting that the highest errors occur at the IV sections close to the cross-section of two irradiance levels or the  $V_{oc}$  of the PV module. Measurement results demonstrate the accurate performance capability of the developed emulator. It is concluded that the maximum power error is less than 4%. Hence, the deployment and measurement procedures are validated.

According to the results obtained in this test, the specifications of the emulator developed in this work are compared with those of the same feature in literature and the commercial products listed in Table 1.

### 3.2. Operation test of the emulator with a PV interfaced to a DC/DC converter

The modeling results of a partially shaded PV module are introduced in Fig. 13. The IV curves are subjected to three- and ten-

substring configurations under similar shading conditions which are depicted in Fig. 13(a) and (b). The modeling routine assumes that covered shaded cells are illuminated at  $500 \text{ W/m}^2$  while the other cells are fully irradiated ( $1000 \text{ W/m}^2$ ).

In general, the three-substring and ten-substring configurations, as shown in Fig. 13(c), exhibit the same IV characteristics at sections near the open-circuit voltage. However, due to the influence of the number of shaded cells and bypass diodes, the IV characteristics corresponding to the two configurations become distinct at the short-circuit area.

In the case of the three-substring configuration denoted by the dashed curves in Fig. 13(c), only the IV curve corresponding to SSN3 exhibits two MPPs. The global MPP which is marked as  $g(3)$  is equal to 158.43 W at 20.11 V. It can be explained that all cells of the left substring are uniformly shaded under  $500 \text{ W/m}^2$  while the other two substrings are exposed to the full irradiation ( $1000 \text{ W/m}^2$ ) and exhibits the same IV characteristics. Due to the activation of the bypass diode connected to the left substring, the dominance of two uniform substring IV characteristics hence causes only two MPPs in this shading scenario.

The three-substring PV module exhibits a single MPP in the cases of SSN1, SSN2, SSN4 and SSN5. The nonuniform irradiation corresponding to the SSN1 of the three-substring configuration results in a single MPP and a more significant slope along the low voltage area (0...10 V). It is not surprising because when a higher current is imposed, a few shaded cells in different substrings exhibit extremely low short-circuit currents compared to their neighbors. The shaded cells operate at the negative

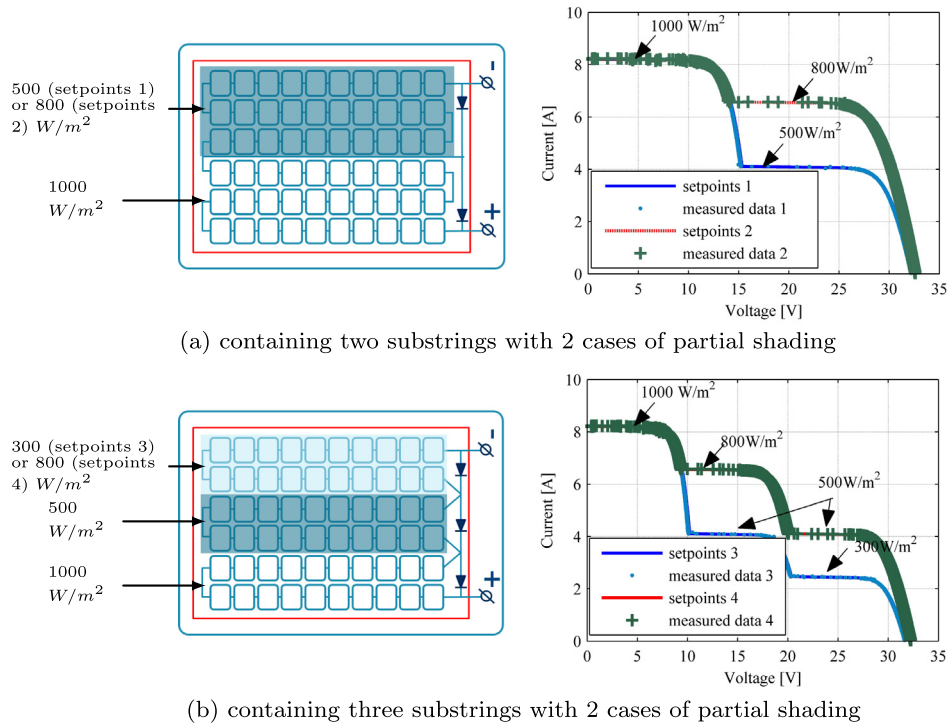


**Fig. 11.** Experimental IV characteristics of the 60-cell PV module KC200GT under partial shading conditions (25 °C) by the developed PV emulator.

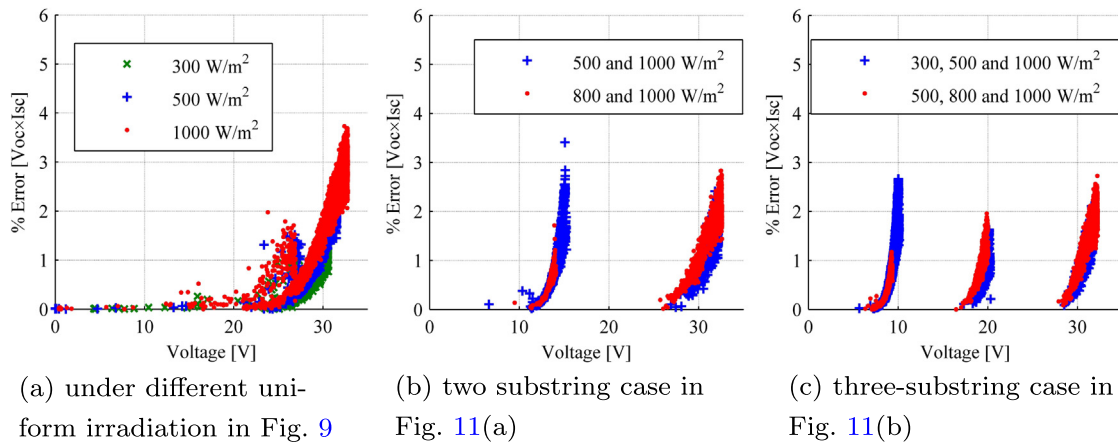


**Fig. 12.** Errors of experimental IV points compared to the modeled characteristics in (a) uniform irradiation, (b) two-substring, and (c) three-substring PV simulation, respectively.

breakdown voltage region (form hot spots), and adversely affect the power production of the substring (Kawamura et al., 2003). Similarly, all three substrings in the scenarios SSN2, SSN4 and SSN5 have the same number of shaded cells while there are no diodes bypassing these shaded cells. As a result, the partially shaded substrings are limited to the current delivered by the partially shaded cells. Therefore, the same drop of the PV module's short circuit current is obtained in Fig. 13(c).

In the case of the ten-substring configuration shown in Fig. 13 (b), the global MPPs of these five shading scenarios, denoting  $g$  (10) in Fig. 13(c), are approximately 133.53 W, 145.04 W, 133.93 W, 133.61 W, and 127.80 W respectively. All five shading scenarios (SSNs) exhibit two MPPs in the ten-substring configuration. While the module's IV curve in the SSN2 has its global MPP near half of the  $V_{oc}$ , the IV curves corresponding to the other four SSNs present the global MPP at the point near  $V_{oc}$ .

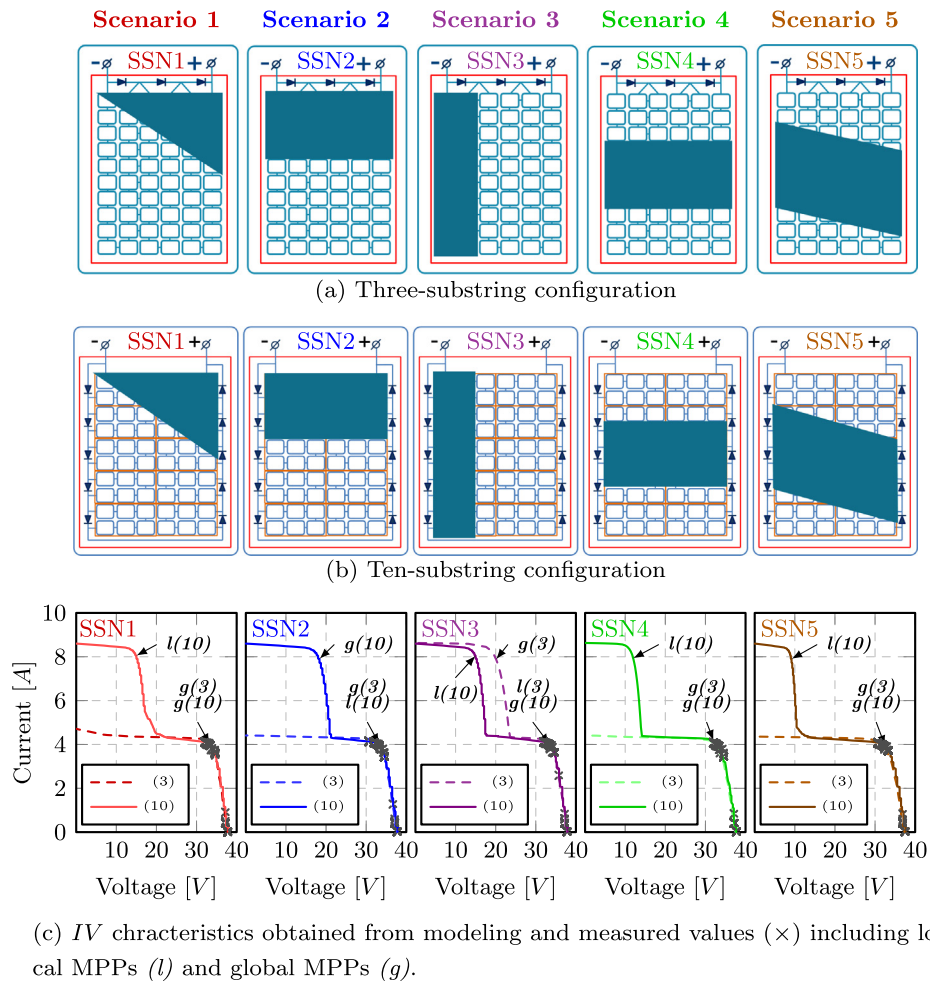
In two scenarios SSN1 and SSN5, while the majority of ten substrings are either fully irradiated or shaded, few of them are under non-uniform irradiation. It is explained that the high current generated by fully irradiated substrings are bypassed via diodes and not absorbed by shaded cells. Therefore, the PV module exhibits two MPPs corresponding to full and shaded irradiance levels. The partial shading over two substrings in the ten-substring configuration causes the hot spot formation. Nevertheless, the number of shaded cells in the partially shaded substrings are different, which results in a smooth PV module curve at 20 V in the SSN1. Similarly, the partially shaded substrings in the SSN5 result in the smooth section of the module's IV curve near 10 V.

Although SSN2, SSN3 and SSN4 have the same number of shaded cells, their IV characteristics in the ten-substring configuration are slightly different. While all substrings of the PV module corresponding to the SSN2 are uniformly irradiated by either

**Table 1**

Comparison with other developed PV emulators with multistring/partial shading emulation.

Parameter	This work	Chroma (2012)	Di Piazza and Vitale (2010)	Koran et al. (2014)	Kadri et al. (2010)
Output voltage [V]	0–120	0–150	0–250	0–200	0–300
Output current [A]	0–13	0–40	0–20	0–20	0–11
Output power [W]	1500	2000	3000	1800	3300
Voltage noise (p-p) [mV]	30	450	N.A.	<2000	300
RMS voltage ripple [mV]	7	65	N.A.	N.A.	100
RMS current ripple [mA]	10	80	N.A.	N.A.	20
Rising time [ms]	12	10	N.A.	N.A.	15.
Falling time [ms]	30	83	N.A.	40	30.
Temperature variation	yes	yes	yes	no	yes
Avalanche breakdown	yes	yes	no	no	no
Partial shading simulation	yes	yes	yes	yes	yes
Cell-level modeling	yes	yes	no	no	no
Data logging	yes	yes	N.A.	N.A.	N.A.
Graphical user interface	yes	yes	N.A.	N.A.	yes

**Fig. 13.** Typical characteristics and measurements of a 60-cell PV module GHSolar165M125 under five shading scenarios where (3) and (10) denote the three-substring (a) and ten-substring (b) configurations respectively; measured points obtained by interfacing the emulator to the ST-EVAL (c).

500 W/m<sup>2</sup> or 1000 W/m<sup>2</sup>, the SSN3 and SSN4 have five and four partially shaded substrings, respectively. The greater number of fully irradiated substrings in the SSN2 compared to the other two scenarios results in the higher inflection voltage (around 20 V), the voltage value at which the associated bypass diodes become active (Petrone and Ramos-Paja, 2011). Despite the same global

MPP exhibited by the IV curve in the SSN3 and SSN4, the inflection voltage in SSN4 is lower.

The laboratory hardware setup is carried out as in Fig. 14. The PV emulator is interfaced to a DC/DC converter ST evaluation board (ST-EVAL) that delivers energy from the developed PV emulator to a 400 V DC bus (STMicroelectronics, 2011). The ST-EVAL adopts the



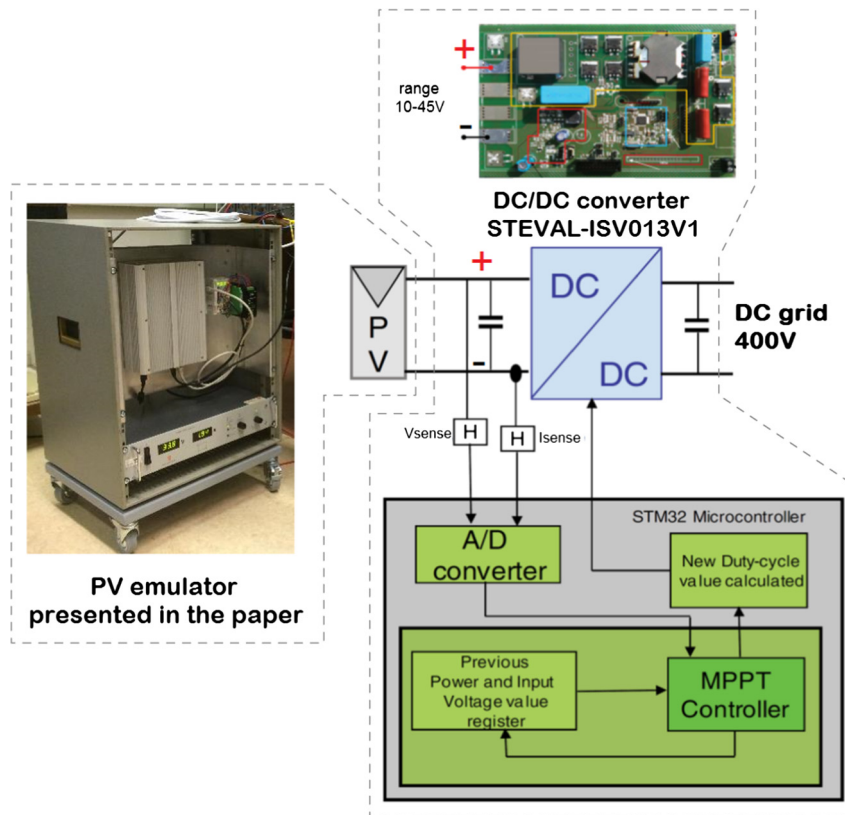


**Fig. 14.** Connection diagram of the hardware setup for testing the PV emulator performance with the PV optimizer demonstration board ST-EVAL-ISV013V1 (STMicroelectronics, 2011).

perturb-and-observe (P&O) algorithm to track the MPPs at given cell temperatures and irradiance levels (Ishaque et al., 2011; Femia et al., 2005).

The emulator emulates both three-substring and ten-substring configurations of a 60-cell PV module to evaluate whether the P&O implemented in STEVAL can converge to global MPPs under different SSNs. Measured *IV* points are denoted by (×) for each sampled measurement. Fig. 13(c) demonstrates that a minority of measured *IV* points distributing around  $V_{oc}$  is due to the start-up procedure of STEVAL. When the MPPT is activated, the majority of measured points in the vicinity of (32 V, 4 A) are located near the local MPP near  $V_{oc}$ . The steady-state operating point associates with the power mismatch in SSN2 of the ten-substring configuration and SSN3 of the three-substring configuration, respectively.

It is proven that the STEVAL board under several shading scenario tests cannot reach the global MPPs, including SSN3 of the three-substring and SSN2 of the ten-substring case. Nevertheless, experimental results illustrate that the PV emulator provides the *IV* curves as modeled, which is verified by the measured points when the emulator interconnects to a power converter such as the STEVAL. In short, the developed emulator can be used to benchmark the operational performance of the power converters at given conditions of substring configurations and partial shading conditions.

#### 4. Conclusion

An emulator for characterizing a multiple substring PV module under partial shading scenarios has been proposed in this paper. The *IV* characteristics of identical substrings in a PV module are obtained by grouping the *IV* characteristics of series-connected cells in each substring, and by imposing bypass diode behavior to

achieve the module characteristics. In this way, modeling the *IV* characteristics of a PV module with a variety of substring configurations and partial shading conditions becomes feasible.

The emulator has been built and experimentally validated by interfacing it to an electronic load and a DC/DC MPPT converter. In the control stage, the KF technique and the hybrid control strategy are implemented to eliminate measurement noises and mitigate the communication latency of control. The proposed control strategy hence enhances the perfect matching among simulated *IV* curves and operating points of the PV emulator output at high-speed responses.

In comparison, together with Chroma (2012), this study outperforms previous ones (e.g. Di Piazza and Vitale (2010), Koran et al. (2014), Kadri et al. (2010)) in terms of modeling (cell-level, avalanche breakdown, partial shading) and controlling (fast-transient, low relative *IV* error). In addition, the developed emulator is better than that proposed in Chroma (2012) because of the lower noise and electric voltage/current ripples.

The emulator developed in this study can support future studies about PV applications under partial shading conditions. Moreover, the output performance advocates future work related to testing the operation of a PV power converter interfaced to multiple-substring PV modules as well as evaluating the controllers integrated in these power interfaces with time- and cost-effectiveness.

#### Acknowledgments

This work has been supported by an internal part of the SBO project “SmartPV” funded by the Flemish Agency for Innovation by Science and Technology (IWT), Belgium. The authors would like to thank Dr. Georgi Yordanov for his constructive suggestions.

## References

- Abidi, H., Ben Abdelghani, A.B., Montesinos-Miracle, D., 2012. MPPT algorithm and photovoltaic array emulator using DC/DC converters. In: Proc. Mediterr. Electrotech. Conf. – MELECON, pp. 567–572.
- Agrawal, J., Aware, M., 2012. Photovoltaic system emulator. In: 2012 IEEE Int. Conf. Power Electron. Drives Energy Syst., pp. 1–6.
- Balato, M., Costanzo, L., Gallo, D., Landi, C., Luiso, M., Vitelli, M., 2016. Design and implementation of a dynamic FPAA based photovoltaic emulator. Sol. Energy 123, 102–115.
- Carrero, C., Ramírez, D., Rodríguez, J., Platero, C.A., 2011. Accurate and fast convergence method for parameter estimation of PV generators based on three main points of the I-V curve. Renew. Energy 36 (11), 2972–2977.
- Chroma, 2012. Programmable DC Power Supply Solar Array Simulation, Model 62000H-S Series.
- Di Piazza, M.C., Vitale, G., 2010. Photovoltaic field emulation including dynamic and partial shadow conditions. Appl. Energy 87 (3), 814–823.
- Díaz-Dorado, E., Cidrás, J., Carrillo, C., 2014. Discrete I-V model for partially shaded PV-arrays. Sol. Energy 103, 96–107.
- Dolan, D.S.L., Durago, J., Taufik, 2011. Development of a photovoltaic panel emulator using Labview. In: Conf. Rec. 37th IEEE Photovolt. Spec. Conf. Seattle, WA, US, pp. 001795–001800.
- Dorf, R.C., Bishop, R.H., 2011. Modern Control Systems. Pearson Prentice Hall.
- Erkaya, Y., Moses, P., Flory, I., Marsillac, S., 2015. Development of a solar photovoltaic module emulator. In: Photovolt. Spec. Conf. (PVSC), 2015 IEEE 42nd. New Orleans, LA, USA, pp. 5–7.
- Femia, N., Petrone, G., Spagnuolo, G., Vitelli, M., 2005. Optimization of perturb and observe maximum power point tracking method. IEEE Trans. Power Electron. 20 (4), 963–973.
- Franklin, G.F., Powell, J.D., Workman, M., 1990. Digital Control of Dynamic Systems. Addison-Wesley.
- Herederó-Peris, D., Capó-Llitas, M., Miguel-Espinar, C., Lledó-Ponsati, T., Montesinos-Miracle, D., 2014. Development and implementation of a dynamic PV emulator with HMI interface for high power inverters. In: 2014 16th Eur. Conf. Power Electron. Appl. EPE-ECCE Eur. 2014. Lappeenranta, Finland, pp. 1–10.
- Ishaque, K., Salam, Z., Syafaruddin, 2011. A comprehensive MATLAB Simulink PV system simulator with partial shading capability based on two-diode model. Sol. Energy 85 (9), 2217–2227.
- Kadri, R., Gaubert, J.-P., Champenois, G., Mostefaï, M., 2010. Real-time emulator of photovoltaic array in partial shadow conditions based on closed-loop reference model. 2010 World Energy Syst. Conf., Targoviste, Romania, vol. 7004, pp. 71–77.
- Kawamura, H., Naka, K., Yonekura, N., Yamanaka, S., Kawamura, H., Ohno, H., Naito, K., 2003. Simulation of I-V characteristics of a PV module with shaded PV cells. Sol. Energy Mater. Sol. Cells 75 (3–4), 613–621.
- Kim, Y., Lee, W., Pedram, M., Chang, N., 2013. Dual-mode power regulator for photovoltaic module emulation. Appl. Energy 101, 730–739.
- Koran, A., LaBella, T., Lai, J.-S., 2014. High efficiency photovoltaic source simulator with fast response time for solar power conditioning systems evaluation. IEEE Trans. Power Electron. 29 (3), 1285–1297.
- Kyocera, 2009. High-efficiency Multi-crystal Photovoltaic Module KC200GT.
- Lu, D.D., Nguyen, Q.N., 2012. A photovoltaic panel emulator using a buck-boost DC/DC converter and a low cost micro-controller. Sol. Energy 86 (5), 1477–1484.
- Martin-Segura, G., López-Mestre, J., Teixidó-Casas, M., Sudrià-Andreu, A., 2007. Development of a photovoltaic array emulator system based on a full-bridge structure. In: 9th Int. Conf. Electr. Power Qual. Util. EPQU 2007. Barcelona, Spain, pp. 1–6.
- Nagayoshi, H., 2004. IV curve simulation by multi-module simulator using IV magnifier circuit. Sol. Energy Mater. Sol. Cells 82 (1), 159–167.
- Patel, H., Agarwal, V., 2008. MATLAB-based modeling to study the effects of partial shading on PV array characteristics. IEEE Trans. Energy Convers. 23 (1), 302–310.
- Petrone, G., Ramos-Paja, C., 2011. Modeling of photovoltaic fields in mismatched conditions for energy yield evaluations. Electr. Power Syst. Res. 81 (4), 1003–1013.
- Quaschnig, V., Hanitsch, R., 1996. Numerical simulation of current-voltage characteristics of photovoltaic systems with shaded solar cells. Sol. Energy 56 (6), 513–520.
- Schofield, D., Foster, M., Stone, D., 2011. Low-cost solar emulator for evaluation of maximum power point tracking methods. Electron. Lett. 47 (3), 208.
- Silvestre, S., Boronat, A., Chouder, A., 2009. Study of bypass diodes configuration on PV modules. Appl. Energy 86 (9), 1632–1640.
- STMicroelectronics, 2011. Appl. Note STEVAL-ISV013V1 250 W DC-DC Solar Module Demonstration Board for Distributed Photovoltaic Architecture.
- Vachtsevanos, G., Kalaitzakis, K., 1987. A hybrid photovoltaic simulator for utility interactive studies. IEEE Trans. Energy Convers. EC-2 (2), 227–231.
- Villalva, M.G., Gazoli, J.R., Filho, E.R., 2009. Comprehensive approach to modeling and simulation of photovoltaic arrays. Power Electron. IEEE Trans. 24 (5), 1198–1208.
- Wandhare, R.G., Agarwal, V., 2011. A low cost, light weight and accurate photovoltaic emulator. In: 2011 37th IEEE Photovolt. Spec. Conf. (PVSC), Seattle, WA, US, pp. 1887–1892.
- Woyte, A., Nijs, J., Belmans, R., 2003. Partial shadowing of photovoltaic arrays with different system configurations: literature review and field test results. Sol. Energy 74 (3), 217–233.
- Yuan, L., Lee, T., Peng, F.Z., Dichen, L., 2009. A hybrid control strategy for photovoltaic simulator. In: Conf. Proc. – IEEE Appl. Power Electron. Conf. Expo. – APEC. Palm Springs, CA, US, pp. 899–903.